

Guided Lamb wave–based structural health monitoring using a novel wave packet tracing method for damage localization and size quantification

Inho Kim and Aditi Chattopadhyay

Journal of Intelligent Material Systems and Structures
2015, Vol. 26(18) 2515–2530
© The Author(s) 2015
Reprints and permissions:
sagepub.co.uk/journalsPermissions.nav
DOI: 10.1177/1045389X15604406
jim.sagepub.com


Abstract

In guided Lamb wave–based structural health monitoring, the interpretation of collected signals is a complex task because of the dispersive and multi-modal characteristics of guided Lamb waves. In this work, a novel wave packet tracing method for damage localization and size quantification is presented. This method involves creating time–space representations of the guided Lamb waves collected at a series of locations with a spatially dense distribution along paths at pre-selected angles with respect to the direction normal to the direction of wave propagation. The fringe patterns due to wave dispersion, which depends on the phase velocity, are selected as the primary features that carry information regarding the wave propagation and scattering. Simulated damage of various sizes, shapes, and locations is analyzed to visually and quantitatively demonstrate the wave packet tracing method.

Keywords

Structural health monitoring, piezoelectric, actuator, sensor

Introduction

In structural health monitoring (SHM), guided Lamb waves (GLWs) have received considerable attention as an effective tool for damage detection because of their inherent advantageous characteristics, such as their ability to propagate over long distances with relatively little energy dissipation, their sensitivity to different types of flaws, and their guiding nature, which enables them to follow curvatures to reach hidden areas (Alleyne and Cawley, 1992; Dalton et al., 2001; Giurgiutiu and Cuc, 2005; Rose, 2004; Wilcox et al., 2001). A significant amount of research has been devoted to developing GLW-based SHM techniques for damage localization and size quantification, and sufficiently accurate results have been obtained in the laboratory using the time-of-flight (ToF) concept (Lemistre and Balageas, 2001; Sohn et al., 2007; Tua et al., 2004; Wang et al., 2004) and advanced signal processing techniques (Das et al., 2005; Giurgiutiu and Yu, 2003; Raghavan and Cesnik, 2007; Taha et al., 2006).

However, challenging problems in the task of damage localization remain, primarily because of the complexity of the characteristics of GLW propagation, such as the multi-modal nature of GLWs, wave

dispersion, and reflections from the finite domain boundaries or unpredictable locations at which damage is present. In previous ToF-based damage localization studies, numerous assumptions have been made, including the following: (1) the time signal can be intuitively separated into individual wave packets, that is, wave packets that do not overlap or overlap only partially and (2) the propagation directions of the individual wave packets are known and thus can be used to identify each wave packet. These assumptions constrain the investigation setup in the sense that the size of the structure must be sufficiently large and the boundaries must be sufficiently far from the actuator–sensor networks. Moreover, the simulated damage must be close to the center of the structure. These restrictions effectively imply conditions in which there is an infinite domain and there are no unwanted reflections. Because of these limitations of ToF-based localization methods,

School for Engineering of Matter, Transport & Energy, Arizona State University, Tempe, AZ, USA

Corresponding author:

Inho Kim, School for Engineering of Matter, Transport & Energy, Arizona State University, Tempe, AZ 85287, USA.
Email: ikim19@asu.edu

studies regarding damage localization for realistically small-sized structures or damage located near boundaries have rarely been conducted.

Early efforts to overcome the problems of multiple modes and wave dispersion include those of Alleyne and Crawley (1991). These authors used the two-dimensional Fourier transform (2D FT) technique to transform multiple time history signals collected at equally spaced locations into the wavenumber–frequency domain to distinguish the multiple modes. Since that time, 2D FT techniques have been utilized in various methods and applications, ranging from numerical modeling (Bartoli et al., 2005; Moser et al., 1999) to experimental approaches (Heller et al., 2000; Lowe and Diligent, 2002).

Recently, several researchers have presented studies that combine the visualization of wavefield measurements obtained using non-contact sensing systems with the 2D FT technique to gain an understanding of GLW propagation; these hybrid methods are known as wavenumber–frequency analysis. Ruzzene (2007) used a surface-affixed piezoelectric transducer (PZT) and a scanning laser Doppler vibrometer (SLDV) as a receiver. Michaels et al. (2011) used a surface-affixed PZT transducer, a scanning air-coupled ultrasonic transducer, and an SLDV. Both studies utilized the 2D FT technique to remove the source wave packets and enhance the signals of waves scattered from induced damage regions. Rogge and Leckey (2013) presented detection results from an investigation of debonding in an aluminum plate and delamination in a quasi-isotropic carbon-fiber-reinforced polymer, which were obtained through both simulations and experiments using a PZT transducer and an SLDV. They used the wavenumber spectrum to visualize waves scattered due to buried damage. Yu and Tian (2013) used a hybrid PZT–SLDV system to obtain wavefield data and distinguished the GLW modes reflected due to induced cracking using a short-space 2D FT. They demonstrated that the 2D FT technique can be used to differentiate the directions of wave packets scattered due to induced cracking in an aluminum plate.

However, the primary disadvantage of the 2D FT technique is that the time component of the time–space domain signal is eliminated by the transform. For damage localization, the time component is essential. Because the 2D FT technique requires prior time–space domain data, sufficient information regarding the multiple GLW modes, the dispersion, and the direction of propagation must be present in the time–space domain data.

In this study, a novel approach that operates in the time–space domain, referred to as the wave packet tracing (WPT) method, is developed to achieve the following objectives: (1) the analysis of complex GLW signals, including multi-path-reflected wave packets; (2) the localization of simulated damage near boundaries; and

(3) the ability to perform both damage localization and size analysis of simulated damage. A time–space representation is used to obtain extensive information regarding the GLW propagation, and the patterns of the GLW packets are used to determine the phase velocity.

This article is organized as follows. First, a brief review of the derivation of the Lamb wave dispersion and the relationship between the group velocity and phase velocity is presented. The time–space representation is described and illustrated to demonstrate the wave dispersion caused by differences between the group and phase velocities. A finite element (FE) simulation is presented in which the patterns of GLW packets in aluminum alloy plates are extracted. Then, the WPT method and its two-step procedure are described. An experimental setup, which is similar to that of the FE simulation and incorporates an acoustic emission (AE) probe and a custom-built linear motion system, is presented for the validation of the time–space representation. The experimental results obtained by applying the WPT method to localize and quantify the sizes of damage regions with various geometries and locations in an aluminum plate, including a rectangular notch, a hole at center of the plate, and three differently shaped notches near the boundary, are presented. Finally, the highlights and limitations of this study are discussed.

Theory of Lamb wave propagation

GLWs are a type of ultrasonic wave that travel along the surface of a thin plate or shell whose upper and lower surfaces are parallel and traction-free. The Lamb wave theory has been fully derived in several previous studies (Achenbach, 1999; Graff, 1991; Rose, 2004). Thus, only the essential details of the Lamb wave equation are presented in this report. Several different approaches can be used to solve the free-plate problem to obtain the Lamb wave equation; the most popular solution methods use displacement potentials and partial-wave techniques (Rose, 2004).

The Rayleigh–Lamb equation is obtained by manipulating the equation of motion of the particle displacements with traction-free boundary conditions (Rose, 2004) as follows

$$\frac{\tan(qh)}{\tan(ph)} = -\frac{(q^2 - k^2)^2}{4k^2pq} \quad \text{for antisymmetric modes}$$

$$\frac{\tan(qh)}{\tan(ph)} = -\frac{4k^2pq}{(q^2 - k^2)^2} \quad \text{for symmetric modes}$$

$$p^2 = \frac{\omega^2}{c_L^2} - k^2 \quad \text{and} \quad q^2 = \frac{\omega^2}{c_T^2} - k^2 \quad (1)$$

where h is the thickness of the plate, ω is the angular frequency, and c_L and c_T are the wave velocities of the longitudinal and shear waves, respectively. Because the

wavenumber k is equal to ω/c_p , where c_p is the phase velocity, the relationship between ωh and c_p can be obtained using numerical methods such as Newton's iterative method. The roots of equation (1) are multiples of the product of the frequency and the plate thickness. Typically, only zeroth-order antisymmetric (A_0) and symmetric (S_0) modes are used in SHM studies to simplify signal interpretation.

Phase and group velocities

The relationship between the group velocity, c_g , and the phase velocity, c_p , is governed by the following equation

$$c_g = \frac{d\omega}{dk} \quad (2)$$

By substituting $k = \omega/c_p$ and $\omega = 2\pi f$ into equation (2), the relationship between c_g and c_p can be obtained as follows

$$c_g = \frac{c_p^2}{\left[c_p - (fd) \frac{dc_p}{d(fd)} \right]} \quad (3)$$

where d is the thickness of the plate. As indicated in equation (3), c_g and c_p are equal only when $dc_p/d(fd)$ is 0. In cases in which c_g and c_p are not equal, wave dispersion occurs. Comparisons of c_g and c_p for zeroth-order modes are depicted in Figure 1. The component waves inside the wave packets propagate either forward or backward because of the difference between c_g and c_p ; this phenomenon is difficult to visualize based on displacement measurements performed at a single point. However, the shape changes inside the wave packets due to wave dispersion are vital for analyzing GLW propagation signals because the center of the wave envelope is most frequently used for calculating the ToF in damage localization methods using various signal processing techniques (Das et al., 2005; Giurgiutiu and Yu, 2003; Raghavan and Cesnik, 2007).

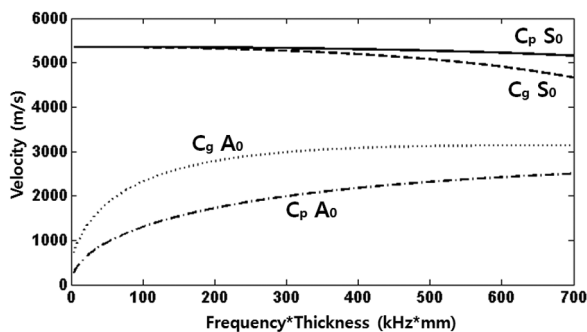


Figure 1. Comparisons of the Lamb wave dispersion between the phase and group velocities of zeroth-order modes in Al6061-T6.

Time-space representation

In this study, a time-space representation is used to visualize the wave dispersion that occurs as waves travel along a thin plate. Time-space representations have also been used in previous studies, such as those by Alleyne and Cawley (1992) and Yu and Tian (2013); however, the primary use of time-space information in previous studies has been to determine frequency-wavenumber relations using the 2D FT. Although frequency-wavenumber analysis can be applied to determine changes in wave directions or to emphasize how various modes interact with damage, it has limited use for damage localization because of the absence of time information in the 2D FT.

To understand and correlate three-dimensional (3D) wave propagation motions with the displacement signals from linearly arranged sensing points, full-field GLW propagation was simulated using an FE model of an aluminum alloy plate with a single, surface-attached PZT. The detailed specifications of the FE model are described in the next section. To construct the time-space representations, the GLW propagation signals were collected sequentially at sensing locations separated by a distance of 1 mm. The axes of the time-space representations are time, collection location, and signal magnitude, as indicated in Figure 2(a). It should be noted that the damping coefficients for the aluminum alloy plate are not included to enable better visualization of the wave dispersions for both modes in the FE simulation.

Using the time-space representation, c_g can be obtained for both modes by computing the slope of the line through the first point of each wave packet in the time signal for each sensor location represented on the vertical axis of the time-space representation. The phase velocity, c_p , can be obtained for both modes from the slope of either a crest or a trough of the component waves, as shown in Figure 2(b). For the S_0 mode, c_p is greater than c_g . Thus, according to the analytical solution for Lamb wave dispersion, as depicted in Figure 1, the component waves inside the wave packet propagate forward. In contrast, c_g is greater than c_p for the A_0 mode; thus, the component waves propagate backward. It should be noted that the velocity difference in the S_0 mode is significantly smaller than that in the A_0 mode; thus, the backward propagation in the S_0 mode is barely visible in the time-space representation at the selected excitation frequency.

Based on observations of the displacement signals at single points, shown in Figure 2(b), it is evident that the shapes of the wave packets in the A_0 mode vary dramatically as a result of wave dispersion. This variation makes it difficult to perform ToF calculations via peak selection in the wave envelopes, and inherent errors can be expected. An alternative approach, based on determining the center of the wave packet via a

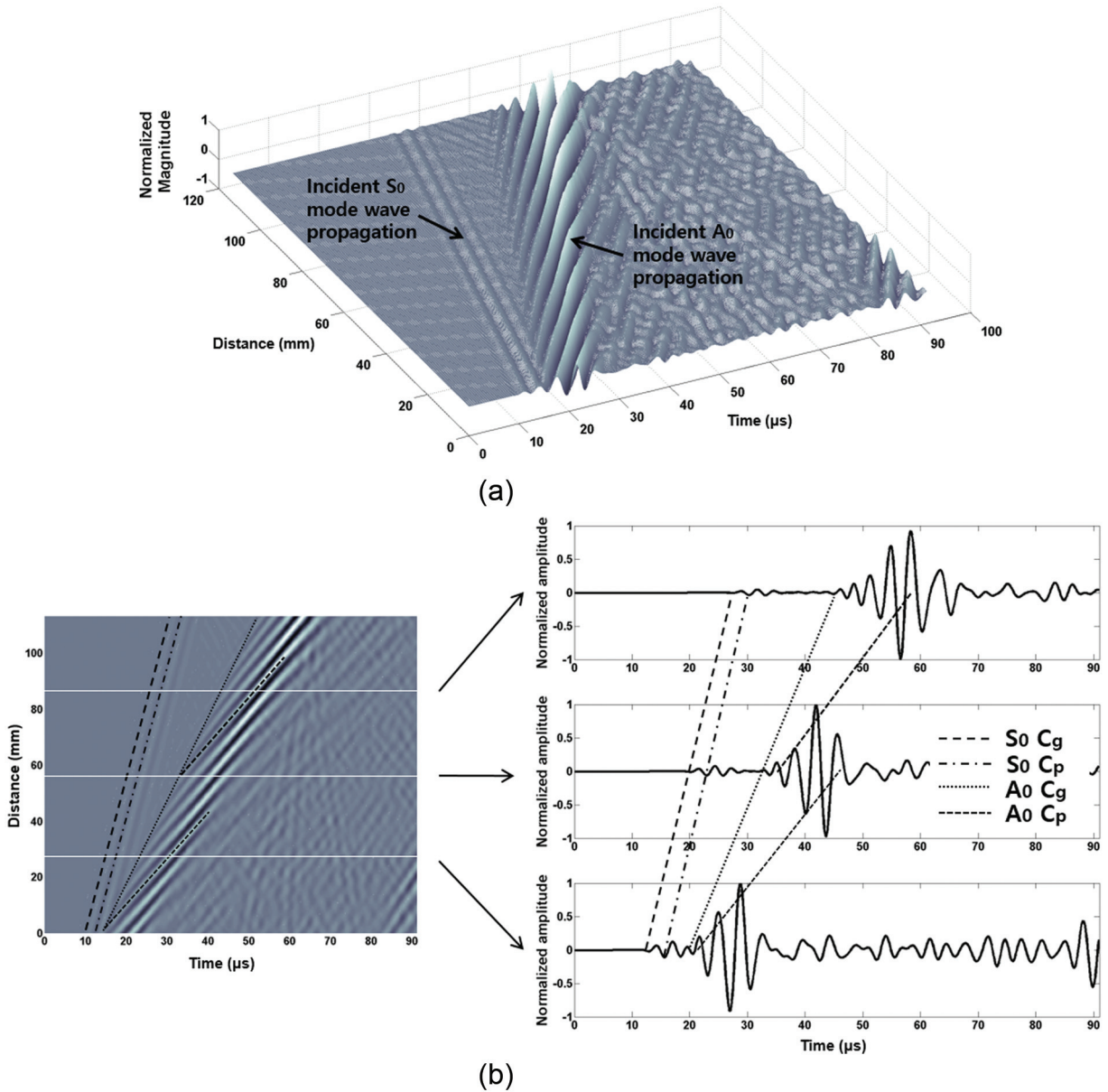


Figure 2. Time–space representation of the out-of-plane Lamb wave displacement at an excitation frequency of 310 kHz: (a) isometric view and (b) top view. From left to right, the dotted lines represent the group velocity of the S₀ mode, the phase velocity of the S₀ mode, the group velocity of the A₀ mode, and the phase velocity of the A₀ mode.

time–frequency analysis, is also a non-trivial method of obtaining a precise ToF calculation because of distortions in the wave packet shapes.

FE model and feature selection

To understand the complex phenomenon of Lamb wave propagation and determine the features to be used for post-processing, 3D FE models were developed in this study using the Abaqus finite element analysis (FEA) commercial software package. An aluminum alloy, 6061-T6, was used as the host structure to simplify the directional variations in wave propagation

features because in this material, c_g and c_p are omnidirectionally constant at the central frequency of the Lamb wave excitation. The dimensions of the aluminum alloy 6061-T6 plate were 300 mm × 300 mm × 2 mm, as indicated in Figure 3(a). Isosceles right triangles with dimensions of 100 mm × 100 mm were trimmed from the bottom-left and top-right corners of the plate to reduce the computational time because wave packets reflected from boundaries do not affect the analyzed signals. A round PZT (APC-850) of 6.35 mm in diameter and 2.5 mm in thickness was modeled for Lamb wave actuation in the Abaqus/Standard analysis. The FE properties of both the

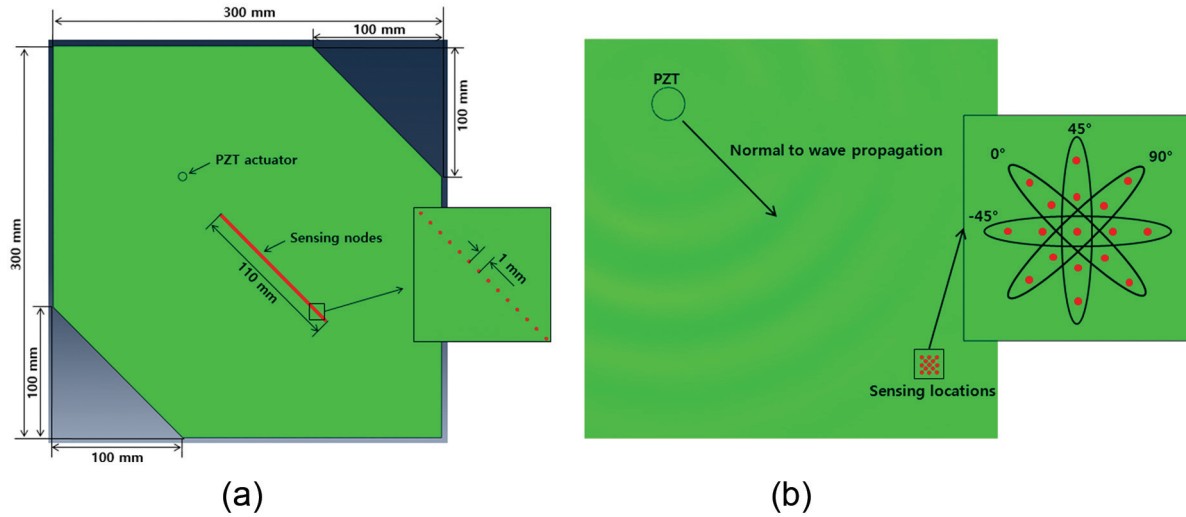


Figure 3. 3D FE model for wave propagation simulations and its dimensions: (a) the sensing path normal to the wave propagation direction used for the time–space representation and (b) sensing paths at various angles (-45° , 0° , 45° , and 90°) with respect to the normal to the wave propagation direction.

aluminum alloy plate and the PZT are provided in Tables 1 and 2, respectively.

The FE mesh size for each model was selected depending on the central frequency of the Lamb wave excitation; the criterion for the mesh size (Δx) was $\Delta x \leq \lambda/20$, where $\lambda = c_p/f$. The value of c_p was determined from the analytical solution for the Lamb wave dispersion curves presented in Figure 1. A 3.5 sine wave modulated with a Hanning window, a tone burst wave, was used as the input signal for PZT actuation. To construct the time–space representation shown in Figure 2,

the wave propagation signals were collected at pre-selected nodes on the top surface separated by 1 mm and arranged in a straight line along the wave propagation direction. In all, 110 sets of out-of-plane displacement signals were collected, as depicted in Figure 3(a), until the time at which the last point of the A_0 group wave packet had passed the last pre-selected sensing point.

Based on the observations of the time–space representation presented in Figure 2, it is clear that the phase velocity patterns always retain their shapes, even though the wave packets are distorted because of the rolling motions of the component waves. To enable the use of these patterns as features for wave propagation analysis, angular variations were introduced into the sensing path to obtain the resulting displacement signals, as indicated in Figure 3(b).

Four excitation frequencies (100, 170, 240, and 310 kHz) were simulated, and the displacement signals

Table 1. Mechanical properties of the aluminum alloy 6061-T6.

Young’s modulus E (GPa)	Poisson’s ratio ν	Density ρ (kg/m ³)
68.9	0.33	2.7×10^3

Table 2. PZT properties.

Elastic properties					
Young’s modulus E (GPa)		Poisson’s ratio ν		Shear modulus G (GPa)	
E1	630	ν_{12}	0.301	G12	235
E2	630	ν_{13}	0.532	G13	230
E3	540	ν_{23}	0.532	G23	230
Density ρ (kg/m ³)		7.5×10^3			
Dielectric constants (F/m)					
D11	$1.51e-8$	D22	$1.51e-8$	D33	$1.30e-8$
Piezoelectric constants (pC/N) (other constants are 0)					
d1 13	d2 23	d3 11	d3 22	d3 33	
590	590	-175	-175	400	

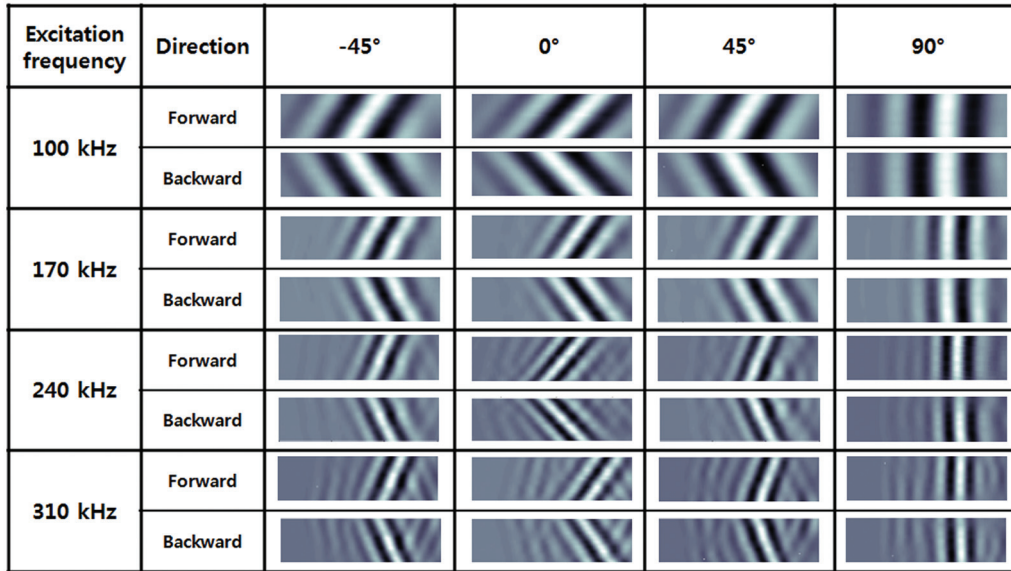


Figure 4. Fringe patterns encoding the wave dispersion.

were sequentially collected at five sensing locations separated by 1 mm. To visualize the displacement signals in the direction opposite to that of the wave propagation, the stacking of the five sensing locations in the time–space representation was inverted.

Figure 4 presents the incident wave packets obtained from the time–space representations of the four sensing paths at different angles. At excitation frequencies of 240 and 310 kHz, the S_0 mode wave packets appear ahead of the A_0 mode packets. Only A_0 mode wave packets are observed at 100 and 170 kHz. The slopes that represent the phase velocity are encoded in the fringe patterns. Interestingly, the inclination of the fringe patterns starts at the phase velocity at the excitation frequency for the 0°-angle sensing path, becomes vertical as the angle is increased to 90°, and then returns to the phase velocity for both the forward and backward sensing paths. The angles of the fringe patterns correspond to the relative angles of the sensing paths; in the WPT method, this relation is used to determine the normal direction of the scattering of waves from the wave generation sources.

WPT method

Previous studies regarding wave scattering have indicated that the interactions of elastic waves with discontinuities, such as structural features, damage, and boundaries, can become local wave sources (Graff, 1991). In this study, the WPT method was developed to determine the locations of these local wave sources based on the fringe patterns that encode the phase velocity and their relative angles for different sensing paths. To quantify the angles in the fringe patterns, a two-step procedure is performed on the time–space

representation images. In the first step, an image processing technique known as the fringe skeletonizing technique, which utilizes the derivative sign binary method (Zhang et al., 2002), is applied to thin the fringe patterns. The derivative sign binary method exploits the facts that the derivatives in the normal direction to a fringe on both sides of its center line have opposite signs, and that the signs of these normal derivatives in the areas between adjacent dark fringes and bright fringe center lines are the same. The derivative sign binary method can be expressed as follows

$$G_{ij} = \begin{cases} 1 & \frac{\partial G}{\partial r} > 0 \\ -1 & \frac{\partial G}{\partial r} < 0 \end{cases} \quad (4)$$

where G_{ij} is the gray level at point ij in the binary image, G is the gray level of the original image, and r is the position vector in the direction perpendicular to the local fringe tangent (Figure 5).

Once the thinning procedure for the fringe patterns is completed, 2D image convolution is performed to determine the angles of the skeletonized fringe pattern. The determination of each angle in the skeletonized fringe pattern using 2D image convolution can be expressed as follows

$$\operatorname{argmax}_{(x,y) \in V} (I * L)[x,y] = \operatorname{argmax}_{(x,y) \in V} \left(\sum_{m=0}^k \sum_{n=0}^j I[m,n] \cdot L[x-m, y-n] \right) \quad (5)$$

where I is the fringe skeletonized image; L is the operator image, which consists of the collection of angles in the lines; k is the width of the image; j is the height of the image; and V is the set that maximizes the similarity between the original image I and the operator L .

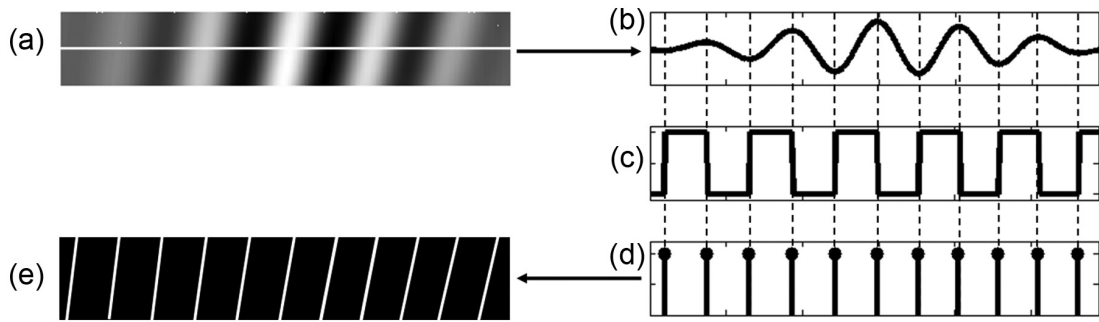


Figure 5. Steps of the fringe skeletonizing technique: (a) fringe pattern, (b) intensity distribution of a cross section of a fringe pattern, (c) derivative sign binary result for (b), (d) fringe skeletons determined by extraction of the boundaries, and (e) sum of the fringe skeletons of the cross sections.

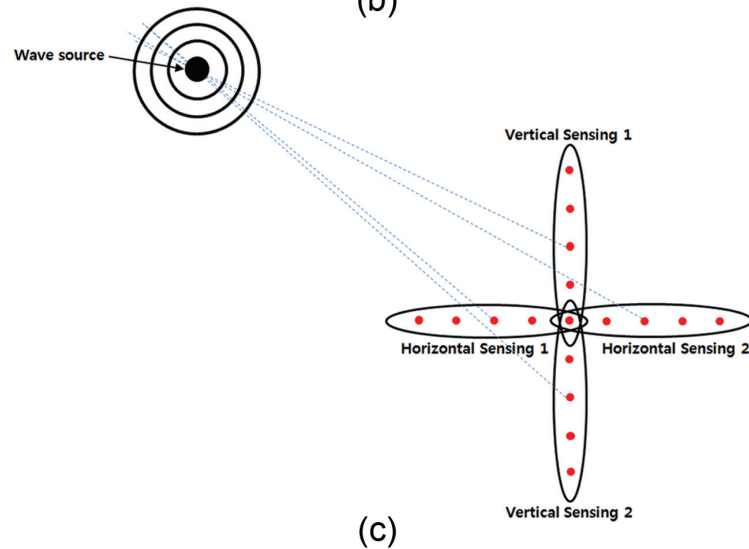
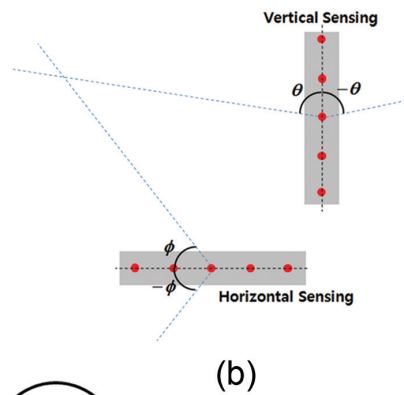
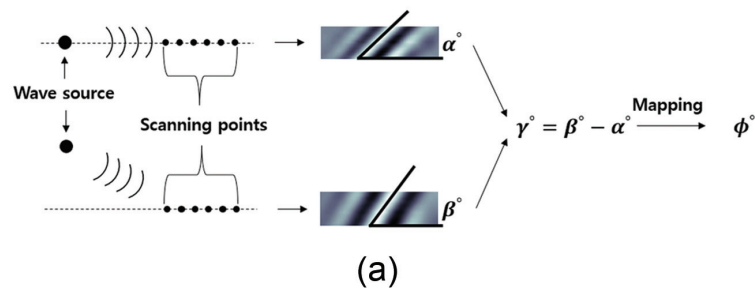


Figure 6. (a) Determining an inclination through the comparison of a reference fringe pattern, α , with an arbitrary fringe pattern, β . The angular difference, γ , is mapped to a real coordinate angle ϕ . (b) Positive and negative angles corresponding to the same inclination. (c) Determining a wave source using the WPT method with a crosshair-shaped sensing scheme.

The output of the image processing technique is a vector expressing the angles corresponding to different times. The angles that compose the vector denote the phase velocities. Therefore, the vector can be converted into another vector of angles with respect to time; these angles represent the directions normal to the wave propagation.

As indicated in Figure 4, the fringe patterns obtained from sensing along a single path represent the same inclinations for both positive and negative angles; this phenomenon is depicted in Figure 6(b). An additional sensing path, which is perpendicular to the original sensing path, is introduced to differentiate the fringe patterns in both half planes. The sensing method used in this study is illustrated in Figure 6(b).

Once M vectors are determined from the vertical sensing paths and N vectors are determined from the horizontal sensing paths, $M \times N$ solutions can be obtained by solving algebraic equations in which the biases are set at the coordinates of the centers of the sensing paths, as indicated in equation (6)

$$\begin{cases} \tan \theta_1(t) \times (x - x_1) + y_1 = y \\ \vdots \\ \tan \theta_M(t) \times (x - x_M) + y_M = y \\ \tan \phi_1(t) \times (x - x_1) + y_1 = y \\ \vdots \\ \tan \phi_N(t) \times (x - x_N) + y_N = y \end{cases} \begin{array}{l} \text{for vertical sensing paths} \\ \\ \text{for horizontal sensing paths} \end{array} \quad (6)$$

where $\theta_M(t)$ and $\phi_N(t)$ are the vectors of the angles with respect to time that represent the vectors normal to the wave propagation direction, x_M and y_M are the Euclidean coordinates of the centers of the vertical sensing paths, and x_N and y_N are the coordinates of the centers of the horizontal sensing paths. The procedure for the WPT method is presented in Figure 7.

In this study, four sensing paths were used to obtain the wave source location; however, additional sensing paths can also be used to increase the accuracy of damage localization. The solutions indicate whether the wave sources are incident wave sources or scattered wave sources. Furthermore, the WPT method can be used to determine the locations of the wave sources of waves reflected from the boundaries. The locations of the wave sources of these reflected waves are placed outside of the inspected structure as virtual points.

Experimental setup

To collect GLW propagation signals in a manner similar to that performed in the FE simulation, an AE probe from Mistras (Micro30s) and a custom-built linear motion system were used. The linear motion system consisted of two sets of linear guides, a linear guide

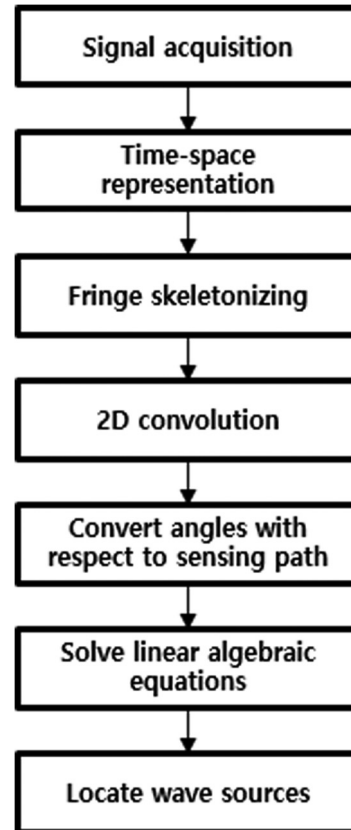


Figure 7. Wave packet tracing method.

bearing, a ball screw, a ball bearing, and a stepper motor. The directions of linear motion were the x -axis, when changing the position of the AE probe, and the z -axis, when bringing the AE probe into contact with the specimen to collect the wave propagation signals. An Arduino microprocessor and a controller system were used to control the stepper motors. The experimental setup is presented in Figure 8. The sensing distance was pre-determined by the relationship between the step angle of the stepper motor and the lead angle of the ball screw per revolution, which allowed the travel distance of the AE probe to be precisely and consistently determined. Various travel distances from 0.65 to 1.5 mm were tested to compare the representation quality of the fringe patterns in the time-space representation, and it was found that varying the travel distance of the AE probe did not affect the results within the investigated range. In this study, the experimental results were obtained with a sensing distance of 0.65 mm because this allowed for the minimal sensor area in the crosshair-shaped sensing scheme. The AE probe was connected to an NI PXI 5105 digitizer to collect signals at a sampling rate of 20 MS/s, and a LabVIEW program was used to calculate and store an average of five collected signals from the AE probe at each collection point. A round PZT with identical specifications to those used in the FE model was used as

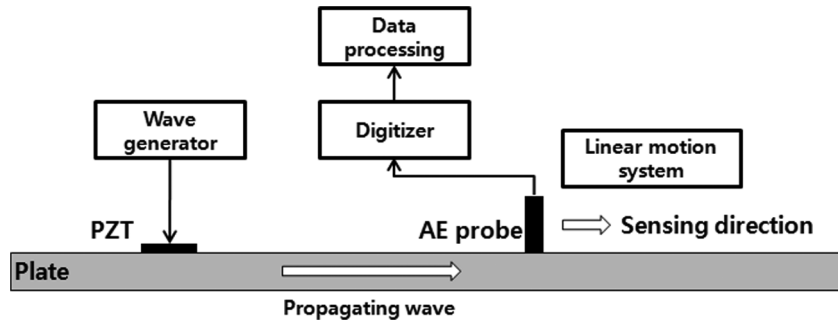


Figure 8. Experimental setup.

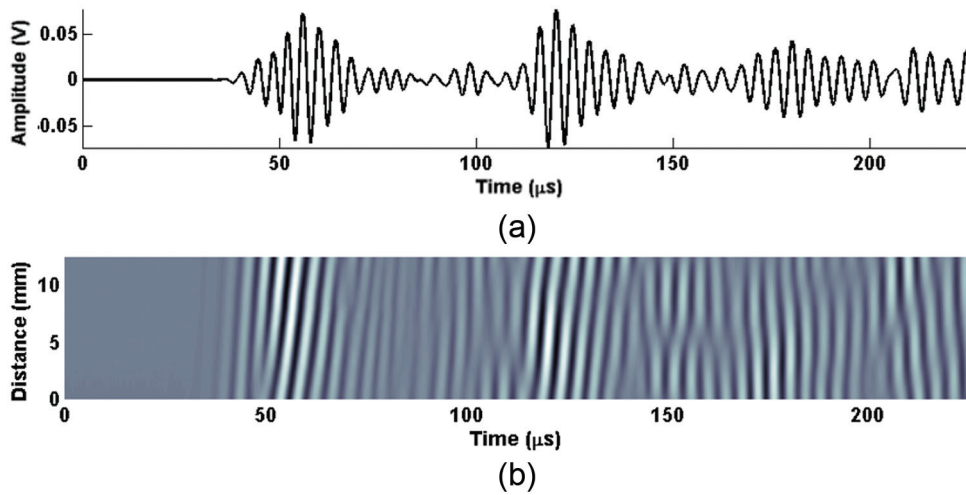


Figure 9. Signal collected using an AE probe at 240 kHz: (a) single-wave response 37 mm from the PZT and (b) time–space representation at locations between 30 and 43 mm from the PZT.

the Lamb wave actuator, and a mixture of FS-A23 resin and FS-B412 hardener from Epoxy Systems, Inc., with a mass ratio of 100:27 was used as the adhesive material to attach the PZT to the host structure. For the validation of the time–space representation and the Lamb wave phase velocity, a plate of aluminum alloy 6061-T6 with dimensions of 254 mm × 254 mm × 2 mm was used. The Lamb wave excitation conditions were identical to those in the FE simulation: a 3.5 sine wave modulated with a Hanning window from 160 to 320 kHz in 20-kHz increments. A PXI 5412 was used to generate the input waveform at a sampling rate of 100 MS/s.

Figure 9(a) presents the signal collected at a single point. Although the first wave packet appears to be a single wave packet, the time–space representation indicates that it is a superposition of two different wave packets. As discussed in the section that introduces the WPT method, the determination of the angles of the fringe patterns can allow these superimposed wave packets to be quantitatively differentiated.

To validate the phase velocities of the experimental and simulated results, the inclinations of the first two fringe patterns were calculated using the WPT method,

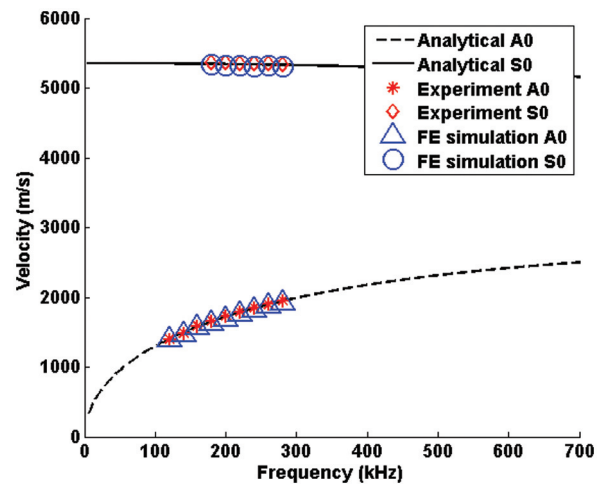


Figure 10. Comparisons of the phase velocities in Lamb wave dispersion obtained from analytical solutions, FE simulations, and experiments within a frequency range of 120–280 kHz.

and the resulting comparisons are presented in Figure 10. Both the experiment and the FE simulation indicate that no S_0 mode wave packets are observed for actuator frequencies of less than 180 kHz.

Damage localization and size quantification results

Damage localization and size quantification for simulated damage regions of various shapes at different locations were conducted using the same experimental

setup and the WPT method. Figure 11 illustrates the division of the experimental plate into nine segments. Ten sensing locations were designated, one in each segment except the center segment, where two sensing locations were allocated to collect time–space information contained in wave reflections from the boundaries. The sensing order was chosen randomly during post-processing to represent the uncertainty present in damage detection. To obtain a sufficient number of wave packets that had been scattered from any existing discontinuities in the plate, the analysis time was cropped until four distinct wave packets were observed in the sensing results from the center segment in the time–space representation.

The specifications of the simulated damage types are summarized in Table 3, and the locations and types of simulated damage are depicted in Figure 12. The damage regions in Cases 1 and 2 damage were located at the center of the plate, with rectangular simulated damage in Case 1 and circular simulated damage in Case 2; these scenarios are illustrated in Figure 12(a). A surface-affixed PZT was located at one corner at a distance of 80 mm from the boundaries to generate the GLWs. The central frequency of the excitation was selected to be 160 kHz to avoid multi-modal complexity, based on the results presented in Figure 10. The

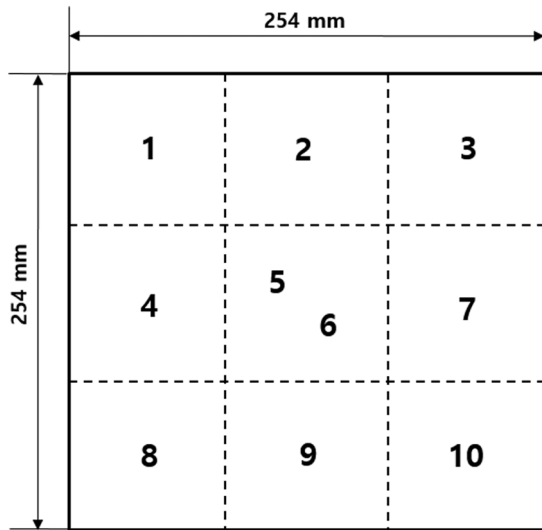


Figure 11. Schematic diagram of sensing locations.

Table 3. Specifications of the simulated types of damage.

Damage cases	Shape	Size	Location
Case 1	Rectangle	5 mm × 2 mm	Center
Case 2	Circle	D5 mm	Center
Case 3	Rectangle	5 mm × 2 mm	Boundary
Case 4	Rectangle	5 mm × 2 mm	Boundary
Case 5	Right triangle	5 mm	Boundary

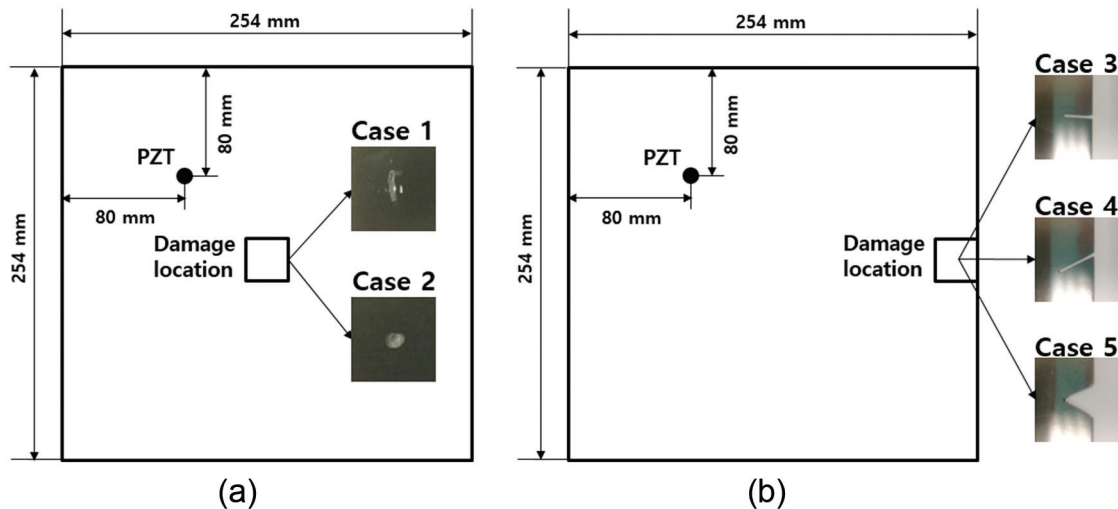


Figure 12. Locations and types of simulated damage: (a) Cases 1 and 2 and (b) Cases 3–5.

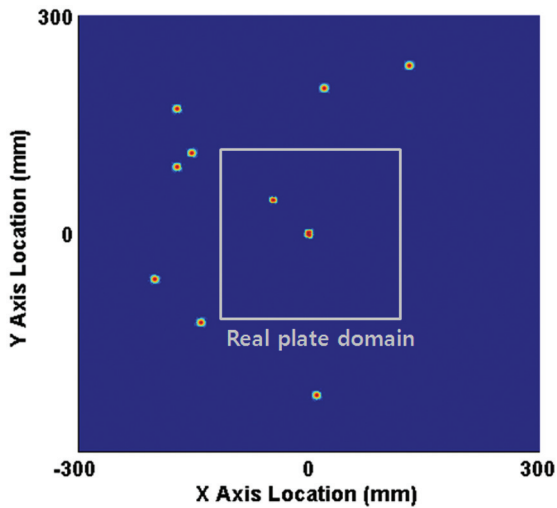


Figure 13. Overlay of the 10 sensing results and the real plate domain for Case 1.

sensing method, which is illustrated in Figure 6(b), involves the collection of signals in both the vertical and horizontal directions at 17 total sensing points per sensing location (9 in each direction), grouped into four sets of 5 sensing points each. In this study, the signals in each group were sequentially collected at a pre-selected spatial sampling interval of 0.65 mm, achieved through adjustments performed using the custom linear motion system, to construct the time–space representations. Figure 12(b) depicts the locations of the simulated damage regions on the boundary of one side of the plate for Cases 3–5. The simulated damage in Case 3 was rectangular in shape and perpendicular to the boundary of the plate. In Case 4, a rectangular damage region of the same size as that in Case 3 was created at a 45° angle to the edge of the plate. The triangular damage in Case 5 was prepared using the same plate

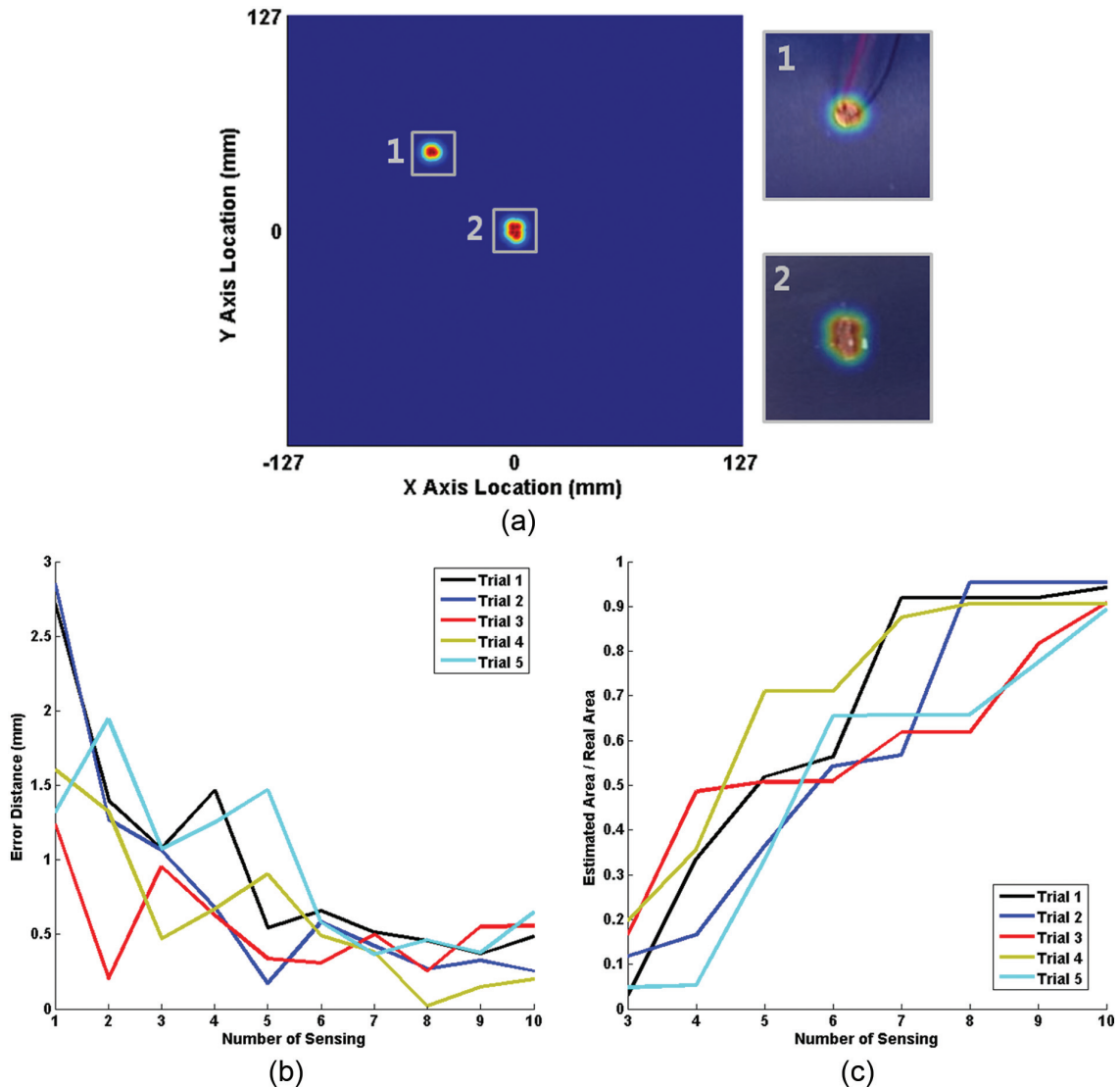


Figure 14. Case 1: (a) wave source localization within the real plate domain and expanded views of (1) the PZT and (2) the rectangular simulated damage region at the center of the plate, (b) the error distance between the estimated and simulated damage locations, and (c) the area ratio between the estimated and simulated damage regions.

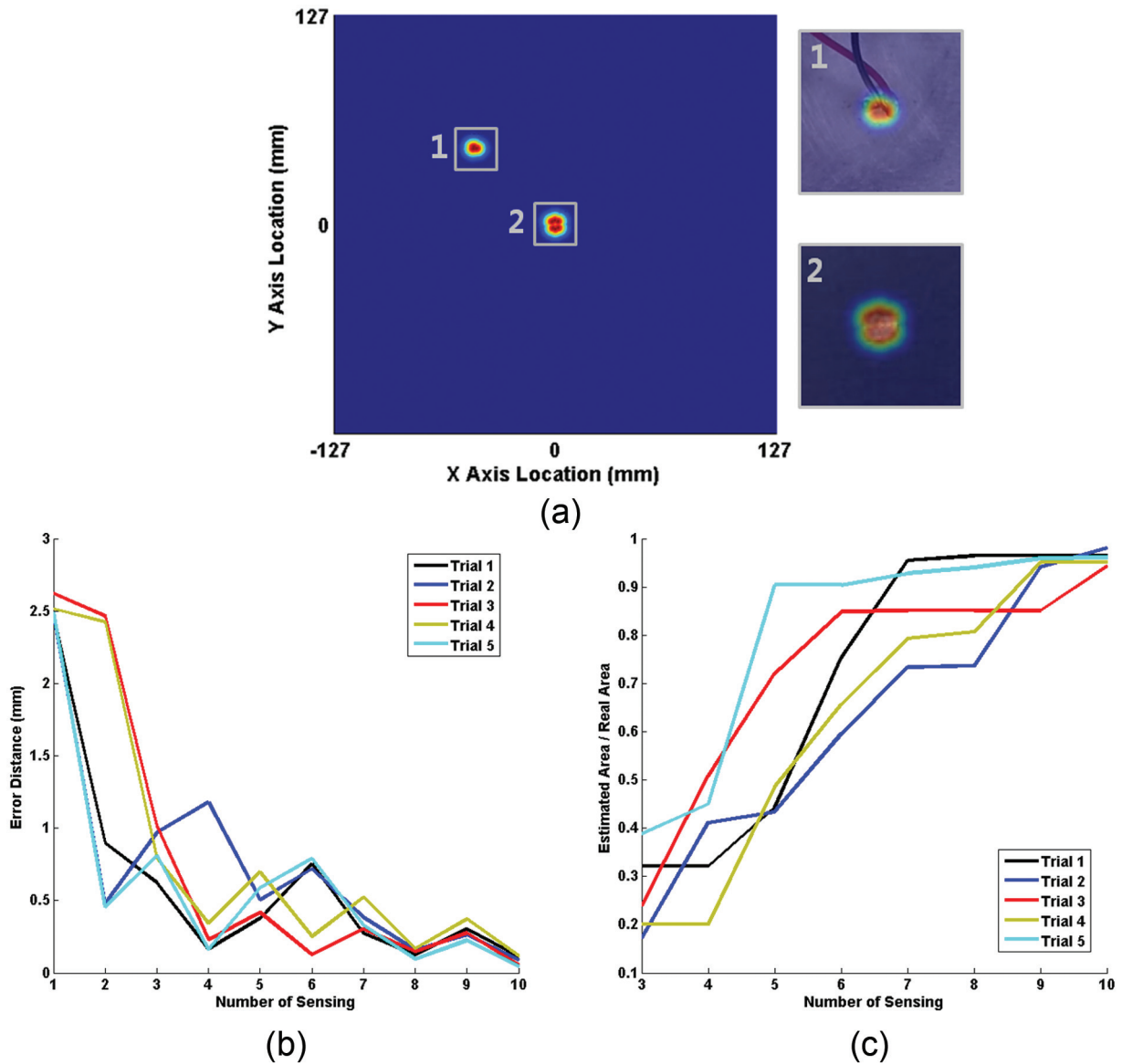


Figure 15. Case 2: (a) wave source localization within the real plate domain and expanded views of (1) the PZT and (2) the circular simulated damage region at the center of the plate, (b) the error distance between the estimated and simulated damage locations, and (c) the area ratio between the estimated and simulated damage regions.

used for Case 4, to which a second 45°-angle cut was applied to create the right-triangular damage region.

Figure 13 presents a unified image of 10 sensing results, for which all wave sources were found using the WPT method within the pre-selected time interval. The errors of $\pm 0.5^\circ$ observed in the 10 sensing trials were introduced into the components of the angle vectors as a Gaussian distribution, and the crossing points determined by solving the $M + N$ linear algebraic equations given by equation (6) are represented as normal distributions. The virtual wave sources due to boundary reflections can be observed outside of the real plate domain.

To quantify the damage localization results obtained using the WPT method, five trials at each of the 10

sensing locations were performed for each investigated damage case. The damage location was estimated using the WPT method by averaging the coordinates of the polygon obtained from the crossing points of the sensing results. The error was then calculated as the Euclidean distance between the estimated and simulated damage locations as a function of the number of sensing locations. Similarly, error analysis of the damage size quantification results was performed by comparing the size of the estimated polygon to that of the simulated damage. The results are presented as the ratio between the estimated and real areas as a function of the number of sensing locations.

After cropping the image to show only the real plate domain and overlapping the configuration of the real

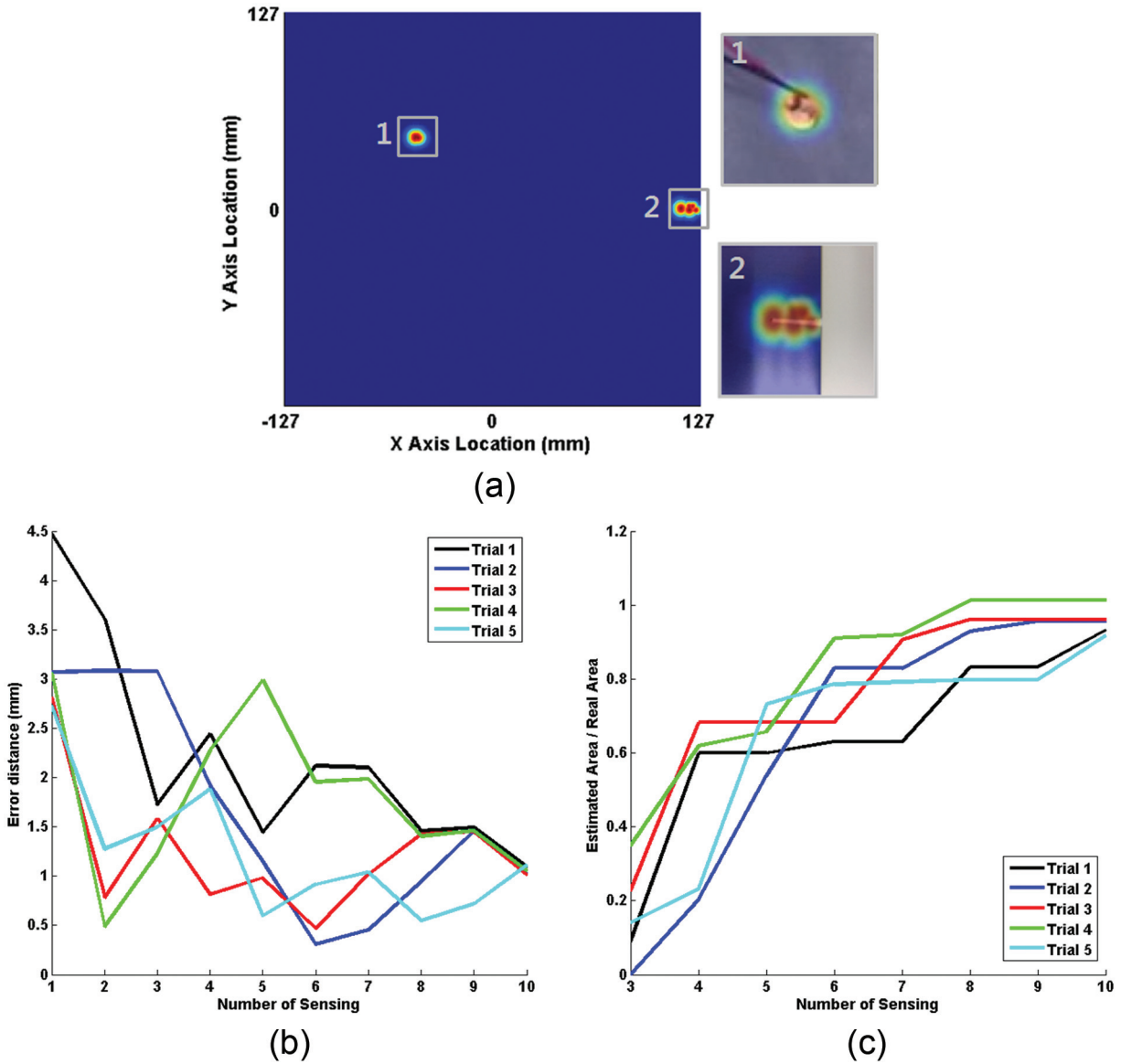


Figure 16. Case 3: (a) wave source localization within the real plate domain and expanded views of (1) the PZT and (2) the rectangular simulated damage region at the boundary, (b) the error distance between the estimated and simulated damage locations, and (c) the area ratio between the estimated and simulated damage regions.

plate, it can be observed that one group of wave sources matches the PZT location, whereas the other group of wave sources is located near the simulated damage region, as indicated in Figure 14(a). For the first group of wave sources (near the PZT), all crossing points lie inside the PZT, as indicated in Figure 14(a-1). Conversely, the wave sources corresponding to the simulated damage are located at the boundaries of the damage region due to either wave reflection or diffraction, as is evident in Figure 14(a-2). Figure 14(b) presents the trend in the error distance between the estimated and simulated damage locations over five trials at each of the 10 sensing locations. It can be observed that the error distances vary slightly among

the trials because of the shape of the simulated damage and the random order of the sensing locations (depicted in Figure 11) at which the measurements were sequentially performed. Figure 14(c) presents the trend in the area ratio between the estimated and simulated damage regions for damage size quantification. For all five trials, the ratio approaches a value of 1 as the number of sensing locations increases.

The results for Cases 1 and 2, in which the simulated damage regions were located at the center of the plate, are presented in Figures 14 and 15, respectively. The error distance for both cases decreases to less than 1 mm as the number of sensing locations increases; furthermore, the area ratio between the estimated and

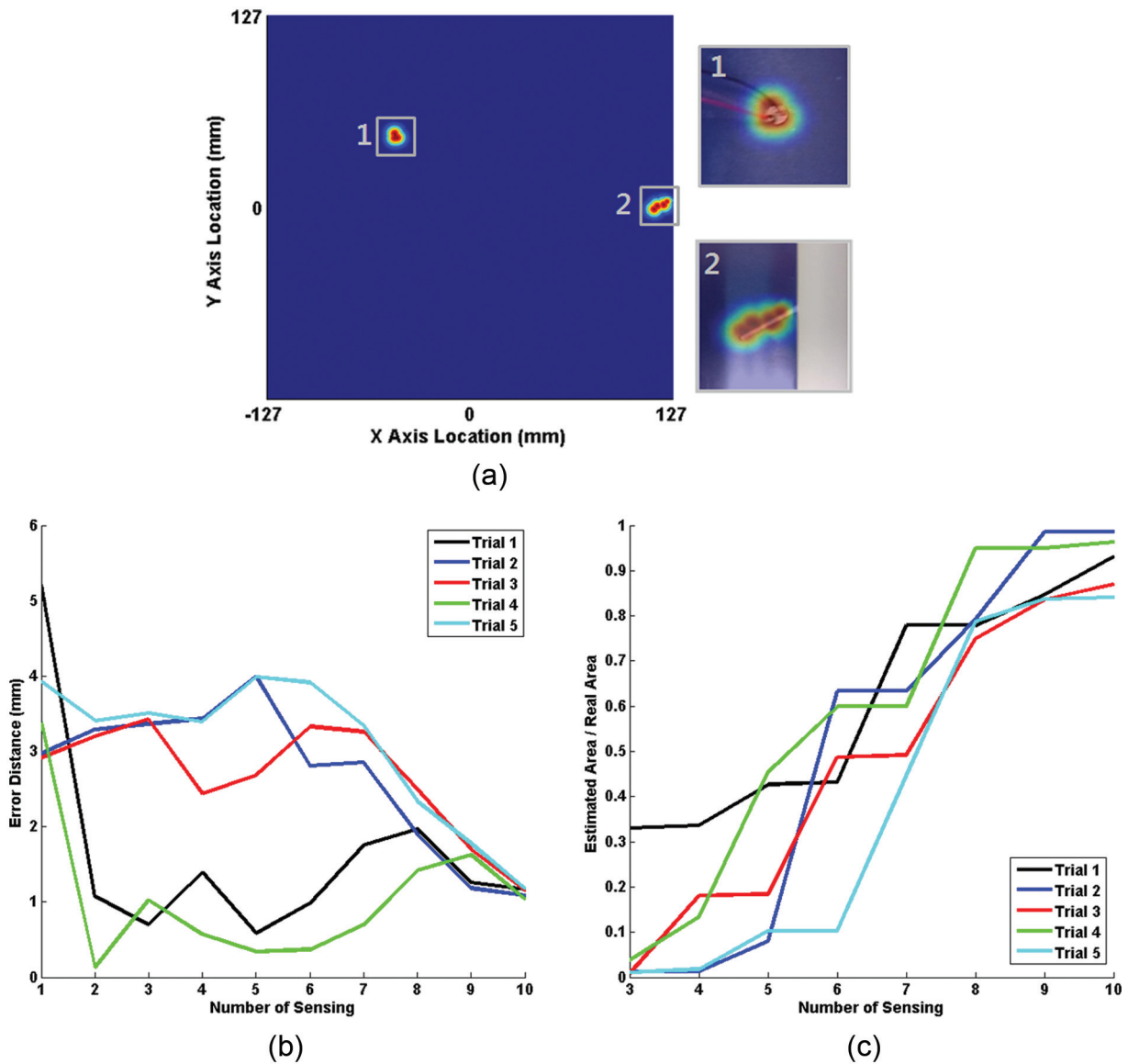


Figure 17. Case 4: (a) wave source localization within the real plate domain and expanded views of (1) the PZT and (2) the 45°-angled rectangular simulated damage region at the boundary, (b) the error distance between the estimated and simulated damage locations, and (c) the area ratio between the estimated and simulated damage regions.

simulated damage regions approaches 1 as the number of sensing locations increases. The circular damage in Case 2 yielded a more consistent decrease in the error distance with an increasing number of sensing locations compared with that in the rectangular damage case because in Case 2, the sources of wave reflection were located around the circumference of the simulated damage region. The results for the simulated damage regions located at the boundary of the plate in Cases 3–5 are presented in Figures 16 to 18, respectively. Because the damage was located at the boundary, the wave packets reflected from the boundary affected the reflected and diffracted wave packets from the simulated damage region. The error distances in these cases are slightly greater than 1 mm, and for all trials, the

area ratios between the estimated and simulated damage regions converge toward 1 when 10 sensing locations are employed.

Regardless of the damage location and shape, the experimental results indicate that the error distance and area ratio tended to converge after measurements were performed at nine sensing locations for all five trials. The area ratio results for a few trials in Cases 4 and 5 are observed to converge more slowly. Because the sensing locations were distributed across the entire plate and placed randomly within each segment, as presented in Figure 11, it was possible for some sensing locations to be located near the boundary of the plate, resulting in poor detection and quantification capabilities. However, as more sensing locations were added,

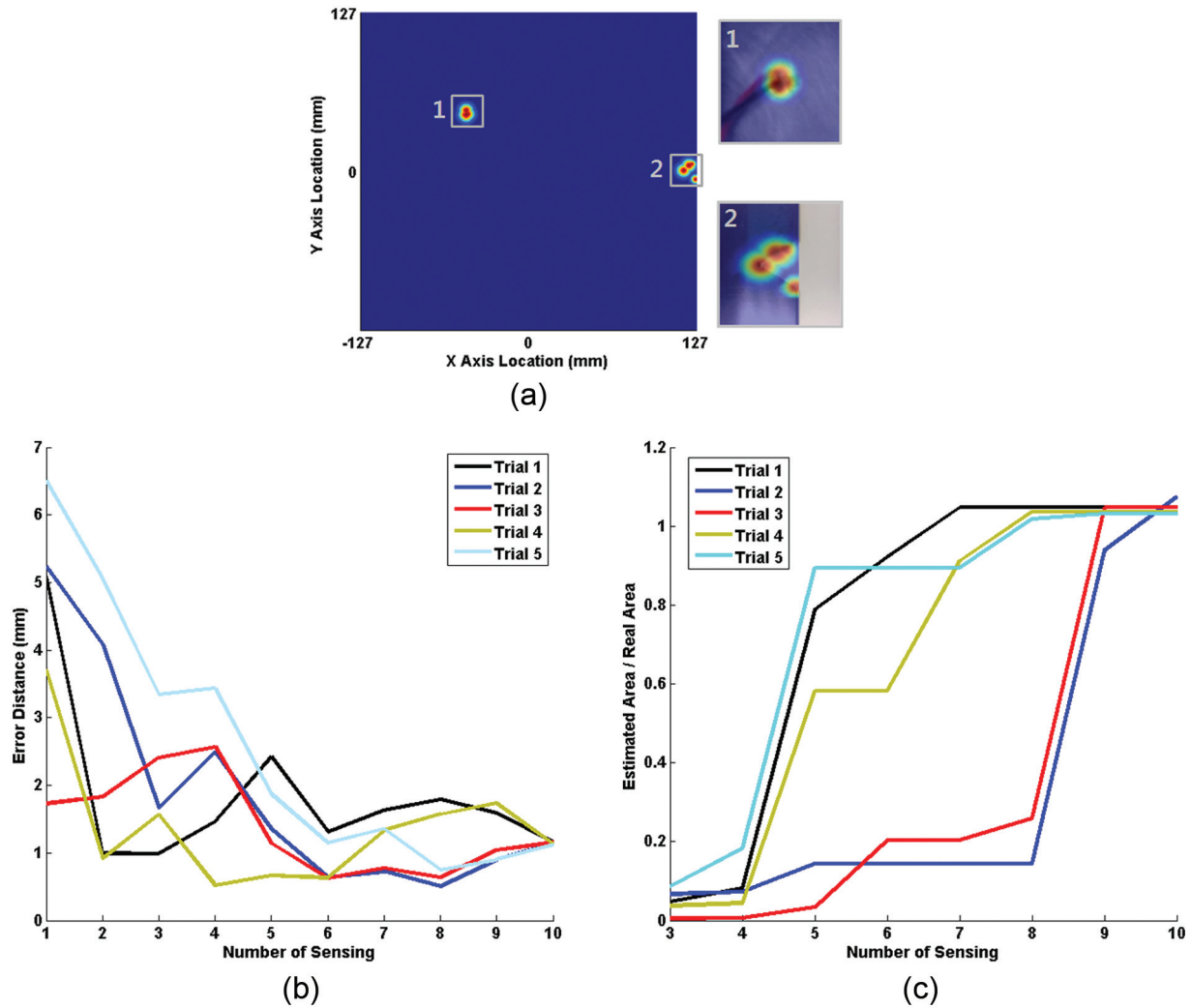


Figure 18. Case 5: (a) wave source localization within the real plate domain and expanded views of (1) the PZT and (2) the triangular simulated damage region at the boundary, (b) the error distance between the estimated and simulated damage locations, and (c) the area ratio between the estimated and simulated damage regions.

the convergence rapidly improved. An alternate strategy for selecting sensing locations by choosing subsequent sensing locations in areas where previous sensing results have indicated unknown wave sources within the plate may allow the necessary number of sensing locations to be reduced.

Conclusion

Damage localization and size quantification are vital tasks in SHM and non-destructive evaluation (NDE). The typical approaches utilize ToF concepts to interpret the signals obtained from transducer and sensor systems, but these methods have limited capabilities in cases of geometrical variations in the inspected structures. Hence, a novel wave packet analysis methodology, called the WPT method, was proposed in this study.

In this method, the full GLW wavefield generated using an FE model is used to gain an understanding of the wave dispersion phenomenon and is represented via a time–space representation obtained using a method based on a spatially dense distribution of sensing points to capture the necessary and sufficient information. The fringe patterns that encode the GLW phase velocities are used to interpret the complex wave scattering caused by the boundaries and damage regions of the structure and to obtain results that can localize and quantify simulated damage of various shapes and locations.

The WPT method can be performed using data acquisition tools that are suitable for use in NDE approaches, such as AE probes with precise motion systems and SLDVs or variations thereof that are designed for spatially dense sensing. For an in situ SHM system, multi-element array transducers and

sensors are potential candidates that can simplify the practical implementation of the proposed method. Because the WPT method uses time-domain data to analyze wave scattering within a selected frequency range to avoid the complexity of mode conversion, further studies regarding time–frequency domain analysis are yet needed.

Declaration of Conflicting Interests

The author(s) declared no potential conflicts of interest with respect to the research, authorship, and/or publication of this article.

Funding

The author(s) received no financial support for the research, authorship, and/or publication of this article.

References

- Achenbach J (1999) *Wave Propagation in Elastic Solids*. New York: North Holland Publishing Company.
- Alleyne D and Cawley P (1991) A two-dimensional Fourier transform method for the measurement of propagating multimode signals. *The Journal of the Acoustical Society of America* 89(3): 1159–1168.
- Alleyne DN and Cawley P (1992) Optimization of Lamb wave inspection techniques. *NDT & E International* 25(1): 11–22.
- Bartoli I, di Scalea FL, Fateh M, et al. (2005) Modeling guided wave propagation with application to the long-range defect detection in railroad tracks. *NDT & E International* 38(5): 325–334.
- Dalton RP, Cawley P and Lowe MJS (2001) The potential of guided waves for monitoring large areas of metallic aircraft fuselage structure. *Journal of Nondestructive Evaluation* 20(1): 29–46.
- Das S, Papandreou-Suppappola A, Zhou X, et al. (2005) On the use of the matching pursuit decomposition signal processing technique for structural health monitoring. In: *Proceedings of the SPIE 5764—smart structures and materials*, San Diego, CA, 6 March, pp. 583–594. Bellingham, WA: SPIE.
- Giurgiutiu V and Cuc A (2005) Embedded non-destructive evaluation for structural health monitoring, damage detection, and failure prevention. *The Shock and Vibration Digest* 37(2): 83. Stanford University, Stanford, CA, September 15–17
- Giurgiutiu V and Yu L (2003) Comparison of short-time Fourier transform and wavelet transform of transient and tone burst wave propagation signals for structural health monitoring. In: *Proceedings of 4th international workshop on structural health monitoring*, Stanford, CA, 15–17 September, pp. 1267–1274.
- Graff KF (1991) *Wave Motion in Elastic Solids*. New York: Dover.
- Heller K, Jacobs LJ and Qu J (2000) Characterization of adhesive bond properties using Lamb waves. *NDT & E International* 33(8): 555–563.
- Lemistre M and Balageas D (2001) Structural health monitoring system based on diffracted Lamb wave analysis by multiresolution processing. *Smart Materials and Structures* 10(3): 504.
- Lowe MJS and Diligent O (2002) Low-frequency reflection characteristics of the S0 Lamb wave from a rectangular notch in a plate. *The Journal of the Acoustical Society of America* 111(1): 64–74.
- Michaels TE, Michaels JE and Ruzzene M (2011) Frequency–wavenumber domain analysis of guided wavefields. *Ultrasonics* 51(4): 452–466.
- Moser F, Jacobs LJ and Qu J (1999) Modeling elastic wave propagation in waveguides with the finite element method. *NDT & E International* 32(4): 225–234.
- Raghavan A and Cesnik CE (2007) Guided-wave signal processing using chirplet matching pursuits and mode correlation for structural health monitoring. *Smart Materials and Structures* 16(2): 355.
- Rogge MD and Leckey CA (2013) Characterization of impact damage in composite laminates using guided wavefield imaging and local wavenumber domain analysis. *Ultrasonics* 53(7): 1217–1226.
- Rose JL (2004) *Ultrasonic Waves in Solid Media*. Cambridge: Cambridge University Press.
- Ruzzene M (2007) Frequency–wavenumber domain filtering for improved damage visualization. *Smart Materials and Structures* 16(6): 2116.
- Sohn H, Park HW, Law KH, et al. (2007) Combination of a time reversal process and a consecutive outlier analysis for baseline-free damage diagnosis. *Journal of Intelligent Material Systems and Structures* 18(4): 335–346.
- Taha MR, Noureldin A, Lucero JL, et al. (2006) Wavelet transform for structural health monitoring: a compendium of uses and features. *Structural Health Monitoring* 5(3): 267–295.
- Tua PS, Quek ST and Wang Q (2004) Detection of cracks in plates using piezo-actuated Lamb waves. *Smart Materials and Structures* 13(4): 643.
- Wang CH, Rose JT and Chang FK (2004) A synthetic time-reversal imaging method for structural health monitoring. *Smart Materials and Structures* 13(2): 415.
- Wilcox P, Lowe M and Cawley P (2001) The effect of dispersion on long-range inspection using ultrasonic guided waves. *NDT & E International* 34(1): 1–9.
- Yu L and Tian Z (2013) Lamb wave structural health monitoring using a hybrid PZT-laser vibrometer approach. *Structural Health Monitoring* 12(5–6): 469–483.
- Zhang D, Ma M and Arola DD (2002) Fringe skeletonizing using an improved derivative sign binary method. *Optics and Lasers in Engineering* 37(1): 51–62.